International Journal of Heat and Mass Transfer 52 (2009) 1158–1166

Contents lists available at ScienceDirect

International Journal of Heat and Mass Transfer

journal homepage: www.elsevier.com/locate/ijhmt

Adaptive phase field simulation of dendritic crystal growth in a forced flow: 2D vs 3D morphologies

C.C. Chen [a], Y.L. Tsai [a], C.W. Lan [a,b,*]

[a] Department of Chemical Engineering, National Taiwan University, Taipei 10617, Taiwan, ROC
[b] Photovoltaics Technology Center, Industrial Technology Research Institute, Hsinchu, Taiwan

ARTICLE INFO

Article history:
Received 23 May 2008
Received in revised form 10 September 2008
Available online 25 November 2008

Keywords:
Adaptive mesh refinement
Phase-field model
Dendritic growth
Solidification
Forced convection

ABSTRACT

Two- and three-dimensional (3D) adaptive phase field simulations of dendritic crystal growth in a forced flow are presented. The simulations are based on an adaptive finite volume mesh for a better resolution on the dendrite morphology. It also allows the simulation in a large domain without much additional computing cost, so that the boundary effect can be neglected for the comparison with classic solutions. With the efficient simulations, the effect of forced convection on the growth behavior at high undercooling is discussed, and the results agree well with Oseen–Ivantsov solution and the reported results. For the case of low undercooling, the simulated tip radius and speed are also consistent with the experimental ones. As compared with 2D morphologies, side branches are easily induced in 3D dendrites, and the dramatic difference can be explained through the simulated flow structures and temperature fields. The effect of the flow on the side branching for different undercoolings is also illustrated.

1. Introduction

The development of microstructures and its underlying mechanisms are important in solidification processing and materials science. For a nucleus in a supercooled melt, as the thermodynamic driving force overcomes the kinetic barrier, it starts growth and the morphology develops. Without the kinetic effect and interfacial energy, the solidification defines the well-known Stefan problem, a diffusive energy balance at the bulk melt and the interface. The first theoretical solution about this solidification problem was given by Ivantsov in 1947 [1]. By ignoring the kinetic effect and interfacial energy, he obtained a prefect parabolic dendrite shape, and the product of the tip radius R and speed V_t is a function of the dimensionless supercooling Δ; $\Delta = C_p(T_m - T_\infty)/\Delta H$, where C_P is the specific heat, T_∞ is the initial temperature of undercooled liquid, T_m the melting temperature, and ΔH the heat of fusion. However, the single equation does not uniquely define a dendrite growth in a given supercooling. With the development of microscopic solvability theory [2–3], the growth operation state of a dendrite can be further defined by the selection parameter σ; $\sigma = 2\alpha d_0/V_t R^2$, where α is the thermal diffusivity and d_0 the capillary length. The selection parameter σ is only affected by the anisotropic strength ε, which is a material property. Also, the anisotropic strength ε plays a critical role in the selection. Without it, the dendrite cannot be selected and grown. The extension of the microscopic solvability theory from diffusive to convective growth was given by Bouissou and Pelce [4]. They applied Oseen flow to develop a relation between tip growth speed and the flow strength, the so-called Oseen-Ivantsov solution, but it is 2D. Therefore, the classic solutions give only the growth operation state of a dendrite. The details of the morphological development of a dendrite growth require a complete time-dependent numerical solution of the Stefan problem coupled with fluid flow and heat transfer. This is extremely challenging especially for 3D simulation using a front tracking method, because of the complex dendrite morphology and the different length and time scales for the interface, heat, and momentum transports.

In recent years, the phase-field model has emerged as a powerful tool for the simulation of solidification with complicated morphologies. In contrast to the front tracking method, the phase field model introduces a continuous phase-field variable ϕ to describe the interface through a rapid transition function. Nevertheless, the diffusive interface approach does not warrant a proper approximation for the Stefan problem with a shape interface unless the interface diffusion length δ is near the capillary one d_0. The thin and semi-sharp interface models developed by Karma et al. [5–8] and Amberg [9] greatly relax the requirement of the diffusive interface thickness, where the interface thickness is allowed be about one tenth of the tip radius. Even so, the simulation of a complex dendrite with a reasonable resolution, while covering the length scales of flow and heat transfer, is still not feasible by using a uniform mesh. Especially, for low supercooling, the

* Corresponding author. Address: Department of Chemical Engineering, National Taiwan University, Taipei 10617, Taiwan, ROC. Tel./fax: +886 2 2363 3917.
E-mail address: cwlan@ntu.edu.tw (C.W. Lan).

0017-9310/$ - see front matter © 2009 Published by Elsevier Ltd.
doi:10.1016/j.ijheatmasstransfer.2008.09.014

Nomenclature

C_p	specific heat
D^*	dimensionless thermal diffusivity
d_0	capillary length
$\vec{e}_x$	unit vector in the x-direction
$\vec{e}_\zeta$	unit vector shown in Fig. 1(b)
ΔH	heat of fusion
$\vec{m}_l^d$	interfacial stress
n	unit normal vector
N_f	number of faces
P^*	dimensionless pressure
P_c	growth Peclet number from classic solution
Pe	growth Peclet number from simulation
P_f	flow Peclet number
Pr	Prandtl number
R	tip radius
Re	Reynolds number
$\vec{S}_f$	surface normal vector of cell face f shown in Fig. 1(b)
T	temperature
T_m	melting temperature
T_∞	initial temperature of undercooled liquid
t	time
U^*	dimensionless flow intensity
u	dimensionless temperature
V_t	tip velocity
$\vec{V}^*$	dimensionless velocity
ΔV	finite volume
w_0	interface thickness
$\Delta x^*_{\min}$	minimum cell size
Δ	dimensionless supercooling

Greek symbols

α	thermal diffusivity
ε	anisotropic strength
κ	tip curvature
ρ	melt density
ν	kinematic viscosity
σ	selection parameter
ϕ	phase-field variable
δ	interface-diffusion length
τ_0	atomic movement
λ	coupling constant
φ	conservation variable

Superscript

*	dimensionless variables

Subscripts

∞	far from the interface
f	at the face
P	at the cell center
Nb	at the neighbor center

computational domain needs to be large enough to avoid the boundary effect. To overcome this, an adaptive grid, with dynamic mesh refining and coarsening, during simulation is required for an efficient simulation.

For 2D adaptive phase filed simulation, some progress has been made by Provotas et al. [10] for diffusive growth and Lan et al. [11] for convective growth. The use of a large domain, Lan et al. [12] have simulated the dendritic growth under a forced flow with various supercoolings. Good agreement with Oseen–Ivantsov solution has been obtained, if the global tip radius is adopted. Recently, Jeong et al. [13–14] have developed a 3D adaptive parallel finite-element code to simulate the solidification of pure materials in a forced flow. The simulated result for low supercoolings was consistent with experimental results [15], but the growth did not reach the steady state. Lu et al. [16] have also simulated the 3D dendritic growth under forced convection, but using a two-mesh approach based on finite difference. Their results are in good agreement with the classic solution for the case of no convection. Although some scattered 3D results have been reported, the one-to-one comparison with 2D simulation has not yet been reported. The growth characteristics of a 3D dendrite in a forced flow have not yet well discussed, and the comparison with 2D cases should provide a deeper insight into the 3D heat flow structure and its effect on the dendritic growth.

In this paper, we present 2D and 3D adaptive phase field simulation using an efficient finite volume method. In addition to the comparison with previous simulations, which are based on different methods, and classic solutions, the simulation at low supercooling is carried out for the comparison with the experimental result. Because of the large thermal and flow boundary layers at low supercooling during experiments, an extremely large domain is required for simulation. Finally, the morphology of 2D and 3D dendritic growth under a forced flow is compared, and then discussed based their flow and thermal fields. In the following section, we shall briefly describe the phase-field model, and then the adaptive finite volume method in Section 3. Section 4 is devoted to results and discussion, followed by short conclusions in Section 5.

2. Mathematical formulation

To simulate a dendrite in a supercooled melt with a forced flow in the x-direction from the upwind direction, the phase field model proposed by Karma and Rappel [5,7] is adopted here. Their model greatly relaxes the stringent requirement on the interface thickness, and is thus very suitable for numerical simulation. The phase field variable φ is set to 1 in the solid, -1 in the melt, and 0 at the interface. The time t is rescaled by τ_0, which characterizes the atomic movement, and the length is rescaled by w_0, which characterizes the interface thickness, and the velocity $\boldsymbol{V}$ is recalled by w_0/τ_0. The temperature T is rescaled to $u = C_p(T - T_m)/\Delta H$. Beside the temperature, the dimensionless variables are denoted with an asterisk superscript unless otherwise stated. Then, the phase field equation can be written as the following:

2.1. Equation of phase-field

$$\begin{aligned} a_s^2(n)\frac{\partial\phi}{\partial t^*} = {} & \left[\phi - \lambda\cdot u(1-\phi^2)\right](1-\phi^2) + \vec{\nabla}^*\cdot\left[a_s^2(n)\vec{\nabla}^*\phi\right] \\ & + \frac{\partial}{\partial x^*}\left[\left|\vec{\nabla}^*\phi\right|^2 a_s(n)\frac{\partial a_s(n)}{\partial(\partial_x\cdot\phi)}\right] \\ & + \frac{\partial}{\partial y^*}\left[\left|\vec{\nabla}^*\phi\right|^2 a_s(n)\frac{\partial a_s(n)}{\partial(\partial_y\cdot\phi)}\right] \\ & + \frac{\partial}{\partial z^*}\left[\left|\vec{\nabla}^*\phi\right|^2 a_s(n)\frac{\partial a_s(n)}{\partial(\partial_z\cdot\phi)}\right], \end{aligned} \tag{1}$$

where $a_s(n) = (1-3\varepsilon)\left[1 + \frac{4\varepsilon}{1-3\varepsilon}(n_x^4 + n_y^4 + n_z^4)\right]$ and $\lambda = \frac{D^*}{0.6267}$; n is the unit normal vector at the interface, D^* is the dimensionless thermal diffusivity ($D^* = \alpha\tau_0/w_0^2$, where α is the thermal diffusivity), and ε_4

the anisotropic intensity. In the above formulation, as discussed by Karma and Rappel [5], the kinetic effect can be neglected and this is realistic for low supercoolings. More importantly, the coupling constant λ and τ_0 need to be carefully chosen according the thin-interface requirement [6].

Furthermore, the dimensionless continuity, energy and momentum equations can be derived, respectively, according Beckermann et al. [17] as the following:

2.2. Equation of continuity

$$\vec{\nabla}^* \cdot \vec{V}^* = 0 \tag{2}$$

2.3. Energy equation

$$\frac{\partial u}{\partial t^*} + \vec{V}^* \cdot \vec{\nabla}^* u = D^* \vec{\nabla}^{*2} u + \frac{1}{2}\frac{\partial \phi}{\partial t^*} \tag{3}$$

2.4. Momentum equation

$$\frac{\partial \vec{V}^*}{\partial t^*} + \vec{V}^* \cdot \vec{\nabla}^* \vec{V}^* = D^* \mathrm{Pr} \vec{\nabla}^{*2} \vec{V}^* - \vec{\nabla}^* P^* + \vec{m}_l^d, \tag{4}$$

where $\vec{m}_l^d = \frac{-2.575\cdot(1+\phi)^2\cdot \mathrm{Pr}\cdot D^*\cdot \vec{V}^*}{4}$ is the interfacial stress [17]. $Pr \equiv \tilde{\nu}/\alpha$ is the Prandtl number, where ν is the kinematic viscosity, and P^* the dimensionless pressure rescaled by $\rho w_0^2/\tau_0^2$, where ρ is the melt density; here, the melt and solid densities are assumed to be the same. In this study, we mainly focus on the dendritic growth in a uniform forced flow in the x-direction. In order to compare with the classic theory and previous calculations, the buoyancy convection due to gravity is neglected, even though it can be added easily in the source term of the momentum equation. The boundary conditions are straightforward for the above equations in the present simulation. The far field temperature is set at the supercooling, i.e., $u = -\Delta$, and the velocity is determined by the stress-free condition (in the y and z directions). The inlet velocity is given to be U^* in the x direction, i.e., $V_x^* = \vec{V}^* \cdot \vec{e}_x = U^*$, where $\vec{e}_x$ the unit vector in the x-direction, and the outflow boundary condition is set by the overall mass balance, assuming that the melt is incompressible.

3. Adaptive finite volume method

The above dimensionless equations and the associated boundary conditions are solved by an adaptive finite volume method. The numerical scheme is very similar to the 2D one we reported before [11–12]. To save space, the scheme is briefly described here. The adaptive finite volume method is first to divide the computational space into a number of finite volumes at grid level 0, i.e., the coarsest mesh. Then, with the need of computation, each volume (the parent cell) can be subdivided into eight (4 for a 2D cell) control volumes (kid cells), defined as the level-1 cells. The mesh refinement can continue by adding more levels to the mesh. Fig. 1(a) shows three meshes at different simulation times. As shown, with the growth of the dendrite, the adaptive mesh refinement (AMR) continues according to the microstructures. On the other hand, for the region losing the physical features, the cells are coarsened to the lower grid level. Constructing the data structure is straightforward by using pointers and derived data types of FORTRAN90. A detailed description of the adaptive data structure and a simple program can be found elsewhere [18].

With the Cartesian finite volume having a number of adjacent cells, as shown in Fig. 1(b), the discrete conservation of a physical quantity for each cell can be derived. First of all, all the previous conservation equations can be written with the following form:

$$a_\varphi \frac{\partial \varphi}{\partial t} + \vec{\nabla} \cdot (b_\varphi \vec{v} \varphi) \vec{\nabla} \cdot (\Gamma_\varphi \vec{\nabla} \varphi) + B_\varphi \Delta V, \tag{5}$$

where φ represents the conservation variable and the corresponding coefficients are summarized in Table 1. Then, for a control cell, with an arbitrary number of neighbors, the finite volume method is to integrate the conservation equation over the finite volume ΔV. After Gauss theorem is applied, for a cell P shown in Fig. 1(b), the flux balance can be written as

$$\left(a_\varphi \frac{\partial \varphi}{\partial t}\right)_P \Delta V + \sum_{f=1}^{N_f} b_{\varphi_f} \varphi_f \vec{v}_f \cdot \vec{S}_f = \sum_{f=1}^{N_f} \Gamma_{\varphi_f} \vec{\nabla} \varphi_f + B_\varphi \Delta V, \tag{6}$$

where P denotes the nodal point at the cell center and f is the mid-location number of the cell face, and $\vec{S}_f$ is the surface normal vector of the face f as shown in Fig. 1(b). The number of faces N_f of each cell can be arbitrary, depending on the refinement or coarsening. The calculation of any variables at the cell face is simplified by distance-weighted interpolation. The main difference in the discretization between AMR and uniform mesh is in the diffusion term, because the normal flux at the face of AMR can not be calculated directly like it in uniform mesh. It comes from that the connector of the P and N_b may not be normal to the cell face. Care also should be taken for the adaptive mesh in the finite volume method, because the vertex points should be avoided for coding simplicity. To do so, the approximation proposed by Mathur and Murthy [19] is adopted. The flux term can be rewritten as

$$\vec{\nabla}\varphi \cdot \vec{S}_f = \frac{\varphi_{Nb} - \varphi_P}{L_{P\_Nb}} \frac{\vec{S}_f \cdot \vec{S}_f}{\vec{S}_f \cdot \vec{e}_\zeta} + (\vec{\nabla}\varphi)_f \cdot \left(\vec{S}_f - \vec{e}_\zeta \frac{\vec{S}_f \cdot \vec{S}_f}{\vec{S}_f \cdot \vec{e}_\zeta}\right), \tag{7}$$

where $\vec{e}_\zeta$ is a unit vector shown in Fig. 1(b).

Further approximation for the time derivative is necessary and the implicit Euler scheme is adopted. Although a higher-order scheme can be used, it needs more memory and computation at each time step. Moreover, in the simulation of dendritic growth, the refined zone is very thin. Hence, the time step is restricted by the amount of interface movement such that the advancement of the new interface needs to be inside the refined zone. Therefore, since time step is small, the first-order Euler scheme is adequate. After assembling the flux balance equations for all cells and imposing the boundary conditions for the boundary cells, one can solve the nonlinear algebraic equations for each time step easily. Due to the incompressibility of the melt, the pressure does not appear explicitly in the equation of continuity. To prevent the checkerboard pressure oscillation, the SIMPLE [20] scheme and the momentum interpolation [21] are further adopted. In addition, the Gauss–Siedel method is used in the inner iterations for solving the linearized equations for all variables.

4. Results and discussion

Because 3D simulation results are quite limited in the literatures, it is important to make sure that our simulations are correct. Therefore, benchmarking with classic solutions and previous results is necessary. The simulation results for discussion are divided into three parts: (1) the comparison with classic solutions and experimental result for low supercooling; (2) the effect of flow on the dendrite morphology and compared with previous simulation results; (3) the comparison of 2D and 3D morphologies. The minimum cell sizes $\Delta x^*_{\min} = 0.4$ and 0.8 are used, respectively, for 2D and 3D simulations.

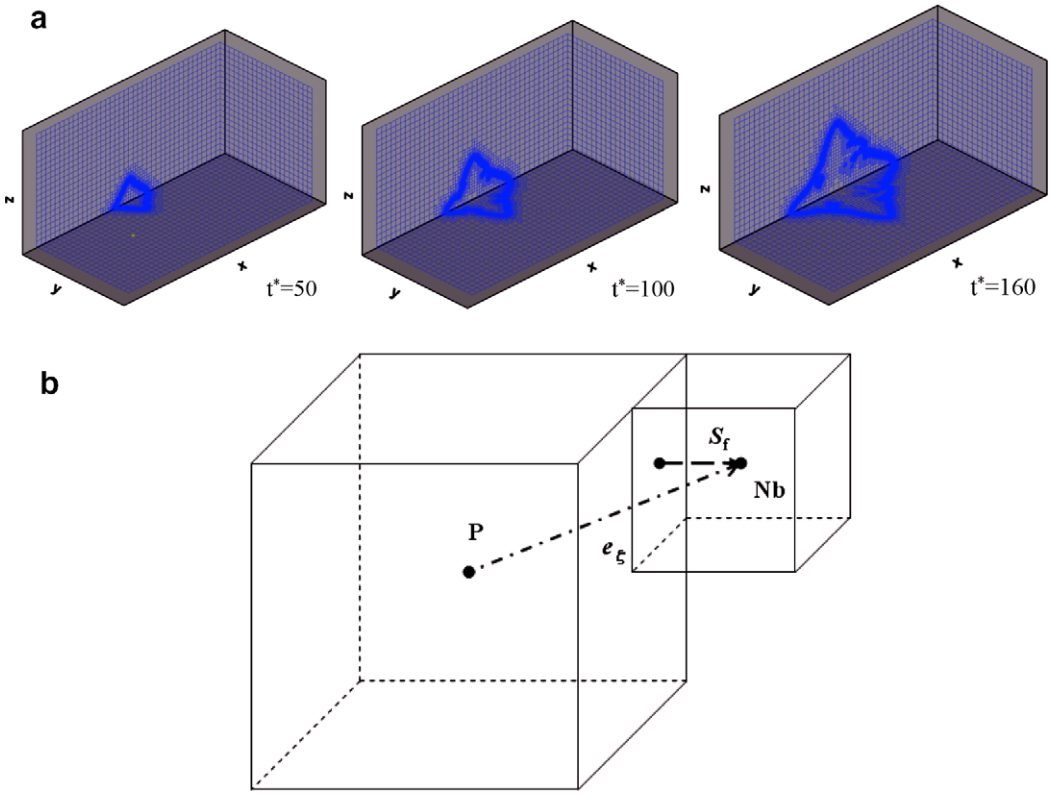

Fig. 1. (a) AMR meshes at different growth times; (b) a schematic finite volume cell for finite volume approximation.

Table 1
The corresponding coefficients for different conservation variables in Eq. (5).

φ	a_φ	b_φ	Γ_φ	B_φ
1	0	1	0	0
$\vec{V}^*$	1	1	D*Pr	$-\vec{\nabla}^* P^* + \vec{m}_l^d$
u	1	1	D*	$\frac{1}{2}\frac{\partial \phi}{\partial t^*}$
ϕ	$a_s^2(n)$	0	$a_s^2(n)$	$[\phi - \lambda \cdot u(1-\phi^2)](1-\phi^2) + \frac{\partial}{\partial x^*}\left[\left\|\vec{\nabla}^*\phi\right\|^2 a_s(n)\frac{\partial a_s(n)}{\partial(\partial x^*\cdot\phi)}\right] + \frac{\partial}{\partial y^*}\left[\left\|\vec{\nabla}^*\phi\right\|^2 a_s(n)\frac{\partial a_s(n)}{\partial(\partial y^*\cdot\phi)}\right] + \frac{\partial}{\partial z^*}\left[\left\|\vec{\nabla}^*\phi\right\|^2 a_s(n)\frac{\partial a_s(n)}{\partial(\partial z^*\cdot\phi)}\right]$

4.1. Comparison with classic solutions and experimental results

To valid the simulation, the comparisons with Ivantsov and Oseen–Ivantsov solutions are considered. The growth Peclet number $P_c = V_t R/(2\alpha)$ and the flow Peclet number $P_f = UR/(2\alpha)$ are defined based on the tip speed V_t and radius R. Because the interfacial tension is considered in the simulation, the local tip radius is not suitable for the comparison with the Ivantsov solution. Instead, the overall tip radius is used by taking a larger portion (about one third) of the dendrite arm into consideration. A fourth-order polynomial is used for fitting the dendrite tip, i.e., $y(x) = ax^4 + bx^2 + c$, where the tip curvature $\kappa(x) = |y''|/(1+y'^{3/2})$ and $R = 1/\kappa$. A sample of fitting result is shown in Fig. 2. As shown, a nice fit is obtained, except very near the dendrite tip, where the shape is affected by the interfacial tension. The 2D and 3D Ivantsov solutions for diffusive growth are available, respectively, as the following:

$$\Delta = \sqrt{P_c}\exp(P_c)\int_{P_c}^{\infty}\frac{e^{-t}}{\sqrt{t}}dt \text{ for 2D} \tag{8}$$

$$\Delta = P_c\exp(P_c)\int_{P_c}^{\infty}\frac{e^{-t}}{t}dt \text{ for 3D} \tag{9}$$

With a forced flow, only a 2D solution is available, which is derived by Bouissou and Pelce [4]. The 2D Oseen–Ivantsov solution can be obtained from the following equation:

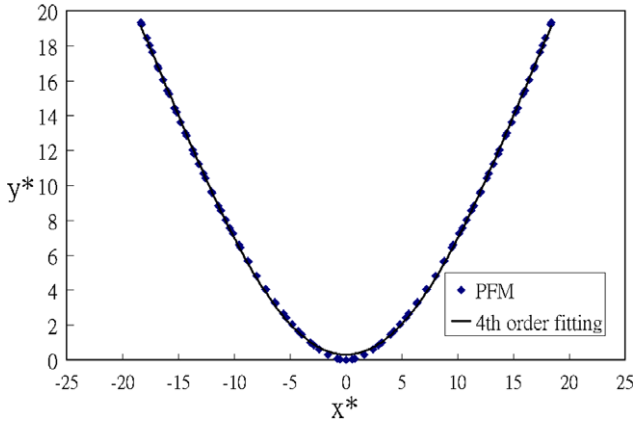

Fig. 2. Fourth-order polynomial fitting of the dendrite tip shape obtained by the phase field model (PFM).

$$\Delta = P_c \exp(P_c - P_f) \times \int_1^{\infty} \frac{\exp\left\{-P_c\eta + P_f\left(2 + \int_1^{\eta}[g(\zeta)/\sqrt{\zeta}]d\zeta - \eta\right)\right\}}{\sqrt{\eta}} d\eta, \quad (10)$$

where

$$g(\zeta) = \frac{\sqrt{\zeta}\,erfc(\sqrt{Re\zeta/2}) + \sqrt{2/(\pi Re)}[\exp(-Re/2) - \exp(-Re\zeta/2)]}{erfc(\sqrt{Re/2})} \quad (11)$$

In the above equation, the Reynolds number Re is defined as $Re = UR/\nu$, where ν is the kinematic viscosity. The above equations can be easily solved by standard numerical methods with care; the numerical integration needs special attention.

The simulation results and the analytical solutions for $\Delta = 0.55$, using P_c vs P_f, are put together in Fig. 3 for comparison. As shown, for the 2D cases, the simulation result is in good agreement with the Oseen-Ivantsov solution. In fact, they are also in good agreement with the previous simulation by Tong et al. [22] and Lan et al. [11] (using a different computer code). For the 3D case, no analytical solution is available for the case with a forced flow. Nevertheless, for the diffusive growth (no flow), the calculated 3D Peclet number is 0.7943, which is very close to the analytical one being 0.7878; the error is 0.81%.

The previous simulations are performed for high supercooling at $\Delta = 0.55$. However, at high supercooling, the dendritic growth is too fast to be observed in the experiments; the crystal growth is hard to control as well. For a well controlled experiment, low supercooling is necessary. However, at low supercooling, the dendrite grows much slower, so that the thermal and flow boundary layers can develop significantly and become much bigger. Therefore, for a well controlled experiment, the domain needs to be large enough. Similarly, it is also true for simulation. An extremely large domain is required for simulation, and this remains a great challenge in computation. The adaptive mesh refinement is powerful in dealing this kind of problem. Jeong et al. [14] made the first attempt to compare their simulated result with the succinonitrile (SCN) experiments by Huang and Glicksman [15]. Here, we also compare our simulation for low supercooling (at small anisotropy) with the experimental observations. In order to compare with the SCN experiment, the anisotropy is set to be 0.0055 and the supercooling $\Delta = 0.04$, which corresponds to about 1°C supercooling in the experiment. At such a low supercooling, $D^* = 116$ is used and the result is shown in Table 2 for comparison. As shown, the result is comparable to the experimental observation and the reported results by Jeong et al. [14]. The difference in the tip velocity and radius are less than 30%.

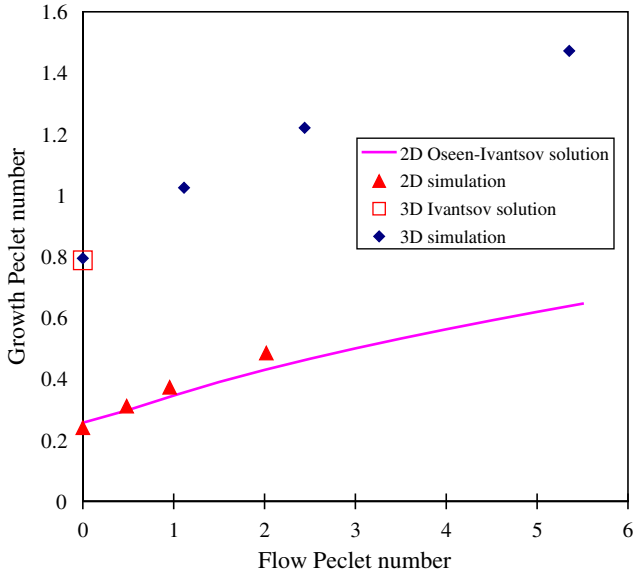

Fig. 3. Comparison of 2D and 3D growth Peclet numbers as a function of the flow Peclet number; $\Delta = 0.55$.

4.2. Effects of forced flow

The effect of forced flow on the 3D dendrite growth was investigated recently by Jeong et al. [13–14] and Lu et al. [16] using an adaptive finite element method and a two-grid finite difference method, respectively. In order to compare their results, two different cell sizes, 0.6 and 0.8, are considered in our finite volume method. The calculated tip velocity and the local tip radius for $\Delta = 0.55$ and $\varepsilon = 0.05$ are compared with previous ones and summarized in Table 3 for diffusive growth first. As shown, the difference with the previous results in the tip velocity is less than 10%. Bigger difference is found for the local tip radius. Because the calculation error for the second derivative is usually large, such a difference for different numerical methods is believed to be reasonable. On the other hand, our comparison with the Ivantsov solution, as shown Fig. 3, is quite good using the global tip radius.

Then, we can examine the effect of flow strength on the dendrite morphology. The simulated cross sections of the morphologies for $U^* = 0$ and 1 are shown in Fig. 4; the simulation result by Jeong et al. [13–14] is put together for comparison; $\Delta = 0.55$, $\varepsilon = 0.05$, $Pr = 23.1$. As shown, they are in good agreement. Some calculated values are summarized in Table 4, and the agreement is good as well. As shown in Fig. 4, the upstream growth is enhanced by the flow, while the downstream tip growth is suppressed by the flow. The overall morphologies at different flow strengths are further illustrated in Fig. 5 for the same supercooling; flow enters from the left with $U^* = 0, 1, 2, 4$ for (a), (b), (c), and (d), respectively. Indeed, with a stronger external flow field, the larger temperature gradients at the upstream are caused by the convective heat flow. This makes the upstream tip grows faster. Furthermore, from the 2D Oseen–Ivantsov solution, the growth Peclet number increases with the flow Peclet number, as shown in Fig. 3, and the 3D growth Peclet number shows a similar trend. The tip's V_tR product increases with the flow intensity U^*.

Again, at the downstream, the heat transfer was suppressed by the flow. Hence, the growth speed decreases with the flow intensity. It is clear that the downstream growth rate for $U^* = 4$ is much slower than that for $U^* = 1$. Table 5 summarizes the tip speeds and tip radii under different flow intensities. The streamlines and the dendrite morphology at $U^* = 4$ are further illustrated in Fig. 6. As

Table 2
Compared with experiment of SCN, $\Delta = 0.04$, $\varepsilon = 0.0055$, $D^* = 116$.

	V_t (cm/s)	R (cm)	Pe	σ
Present	0.0209	1.41×10^{-3}	0.0132	0.0139
Jeong et al. [14]	0.02589	0.97×10^{-3}	0.01126	0.0236
Experiment [15]	0.0170	1.20×10^{-3}	0.0091	0.0238

Table 3
Calculated tip velocity, radius, Peclet number, and scaling parameter for the case of no convection; $\Delta = 0.55$, $\varepsilon = 0.05$, and $D^* = 4$; the morphology is shown Fig. 4.

	Jeong et al. [13] $\Delta x^*_{min} = 0.8$	Lu et al. [16] $\Delta x^*_{min} = 0.8$	Present $\Delta x^*_{min} = 0.8$	Present $\Delta x^*_{min} = 0.6$
V_t^*	0.915	0.883	0.835	0.88
R^*	2.905	3.002	4.33	3.77
P_c	0.332	0.332	0.452	0.415
σ	0.144	0.139	0.071	0.089

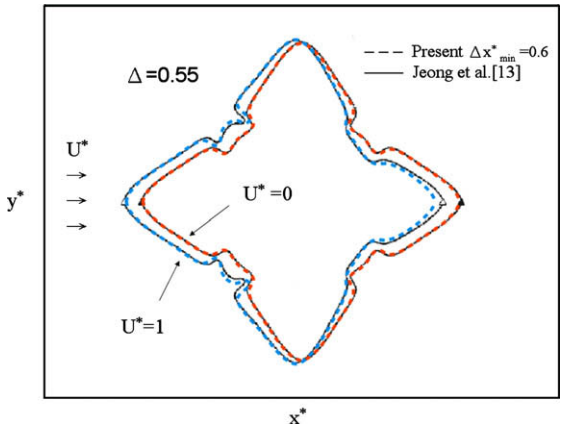

Fig. 4. Comparison of the simulated morphologies with the results by Jeong et al. [13]; red: conduction only ($U^*=0$); blue: with convection ($U^*=1$); $\Delta=0.55$. (For interpretation of the references to colour in this figure legend, the reader is referred to the web version of this paper.)

Table 4
Calculated tip velocity and radius under a forced flow ($U^*=1$ and $t^*=100$); $\Delta=0.55$, $\varepsilon=0.05$, $D^*=4$, and Pr = 23.1; the morphology is shown Fig. 4.

	Jeong et al. [13] $\Delta x^*_{min}=0.8$	Lu et al. [16] $\Delta x^*_{min}=0.8$	Present $\Delta x^*_{min}=0.8$	Present $\Delta x^*_{min}=0.6$
$V_t{}^*$(upstream)	1.038	0.9697	0.92	0.98
$V_t{}^*$(downstream)	0.8		0.65	0.69
R^* (upstream)	3.5	3.739	5.0	4.3
R^* (downstream)	2.41		3.7	3.2

shown, with the convective flow, more side branches are induced and grow toward the upstream; the side branches grow from the side arms. On the other hand, no side branch is induced in the downstream. The side branching induced in 2D cases as discussed in Lan et al. [11–12] is perpendicular to the flow direction and they are induced from the upstream arm; no side branches appear in the side arms. Nevertheless, the side branches appear from the side arms in our simulation is consistent with the simulated result by Jeong et al. [13].

Table 5
The effect of flow intensity U^* on the tip velocity and radius ($\Delta x^*_{min}=0.8$); $\Delta=0.55$, $\varepsilon=0.05$, $D^*=4$, and Pr = 23.1.

	$U^*=1$	$U^*=2$	$U^*=4$
$V_t{}^*$(upstream)	0.92	1.0	1.1
$V_t{}^*$(downstream)	0.65	0.44	0.14
R^* (upstream)	5.0	5.6	7.1
R^* (downstream)	3.7	3.5	Not steady

4.3. Comparison of 2D and 3D growth morphologies in the forced flow

So far, we have made extensive comparison with the classic solutions and previous simulations. However, there is no report for the one-to-one comparison of 2D and 3D growth morphologies and heat flow structures. The effect of the flow on the 2D and 3D growth Peclet numbers has been shown in Fig. 3. As shown in Fig. 3, even without the flow, the 3D growth Peclect number is several times of the 2D one. With the external flow, the trend remains about the same. However, for the 2D case, the deviation of the simulated growth Peclet number from the analytical one (the Oseen–Ivantsov solution) increases with the increasing flow Peclet number. This is due to the effect of side arm and side branches, so that the flow and thermal fields near the upstream tip start to depart from the parabolic shape. Similar is true for 3D cases.

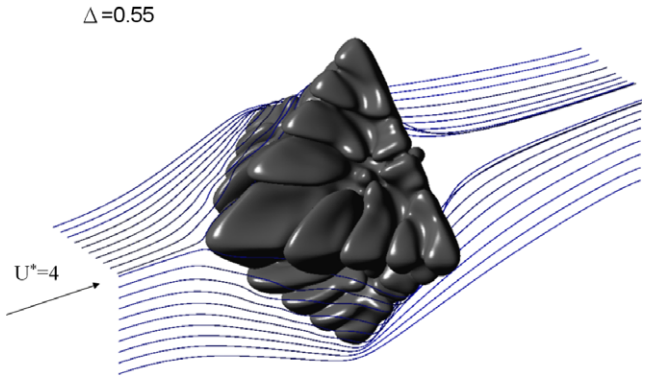

Fig. 6. Flow streamlines and morphology at $U^*=4$.

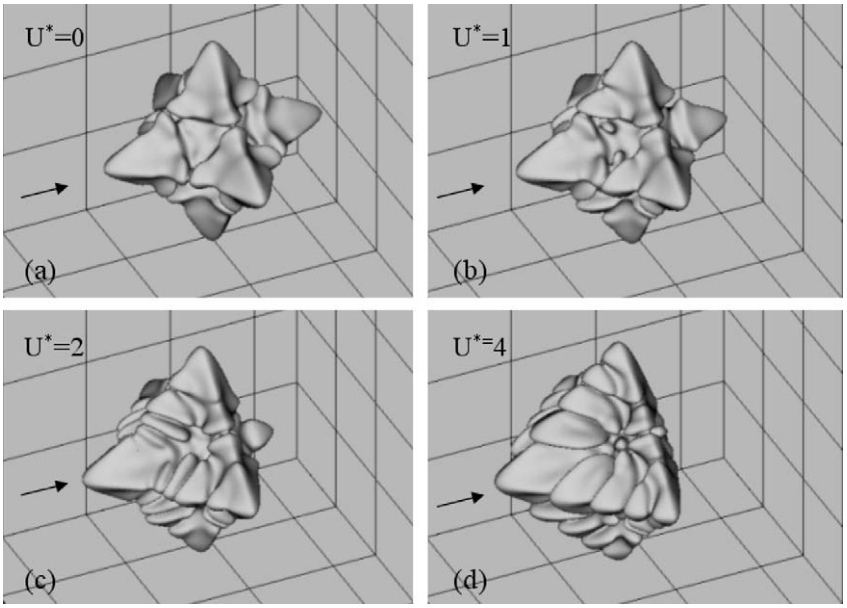

Fig. 5. The effect of flow intensity on the 3D dendrite morphology: (a) $U^*=0$; (b) $U^*=1$; (c) $U^*=2$; (d) $U^*=4$.

For $U^* = 4$ and $\Delta = 0.55$, the cross section of the 2D and 3D morphologies are put together for comparison in Fig. 7(a). As shown, beside the bigger dendrite, more side branches from the transversal arms are induced in the upstream side for the 3D dendrite. However, the 2D side arms remain smooth. The slightly wavy back side also appears in the 3D dendrite, and its growth speed is lower than the 2D one. The flow streamlines of 2D and 3D near the back side are further highlighted in Fig. 7(b) and (c), respectively. As shown, even though the flow behind the crystal is very weak, the 2D and 3D flow patterns are very different. In the 2D flow, not all the fluid behind the downstream crystal flows away the crystal. A small part of the flow near the tail forms vortices. However, in the 3D flow field, no vortex is form.

Beside the flow field, as shown in Fig. 7(d) and (e), the 2D and 3D thermal fields are also quite different. Near the upstream, the 3D temperature contours are much denser than 2D ones indicating much higher thermal gradients near the upstream arms. Since the fluid flows near the dendrite in the 2D dendrite must pass through the dendrite completely, the fluid near the transverse arm always comes from the upstream arm. It means that the fluid near the transverse arms is warmer due to the released heat of fusion during solidification, and thus having smaller temperature gradients. The 2D temperature contours show the largest temperature gradients appear at the upstream tip, and the temperature gradients decrease along the streamline around the crystal. On the contrary, the 3D temperature contours are always denser alone the crystal at the upstream. This is because the fluid near the transverse arm comes from the upstream directly. The flow comes to the dendrite tip can go either in the y direction or the z direction. Hence, the growth of the transverse arm is less affected by the melt flow from the upstream arm. This kind of temperature fields also make the side branches of the transverse arms to grow about as fast as the upstream arm.

The most significant difference of 2D and 3D morphologies in a forced flow is the side branches. In 2D simulations [11,12], the side branches which are perpendicular to the flow appear from the up-

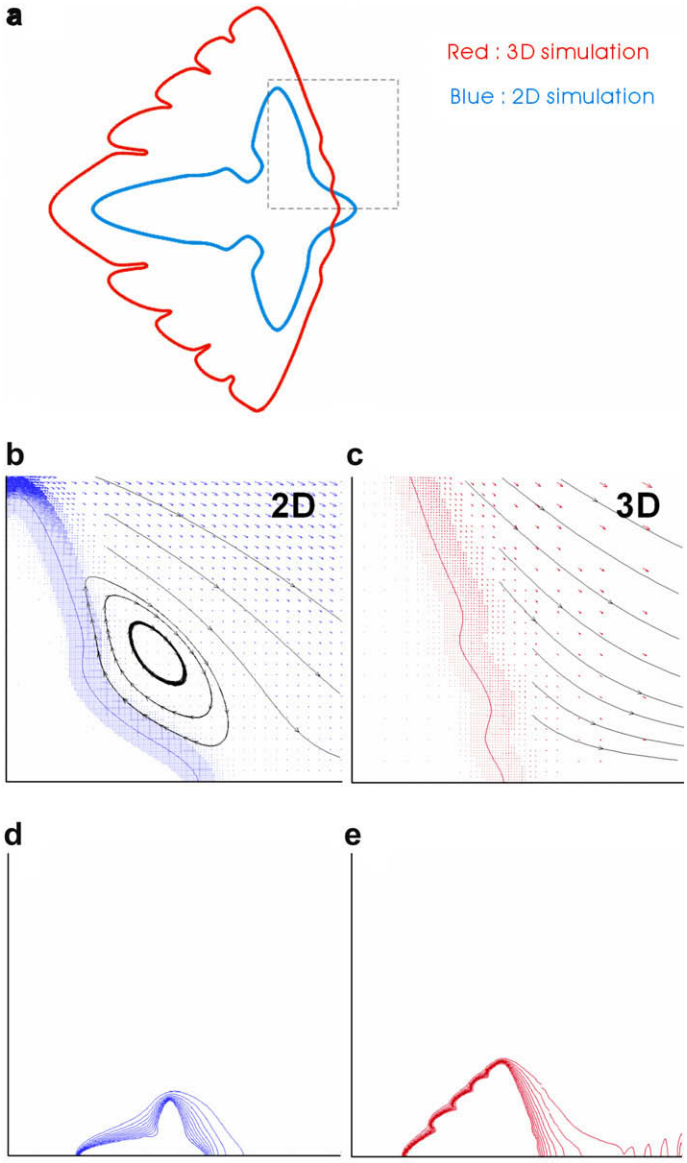

Fig. 7. Comparison of 2D and 3D heat flow and morphologies for $U^* = 4$: (a) 2D and 3D morphologies under forced convection; (b) 2D downstream flow (c) 3D downstream flow ($z^* = 0$) (d) 2D thermal field (e) 3D thermal field ($z^* = 0$).

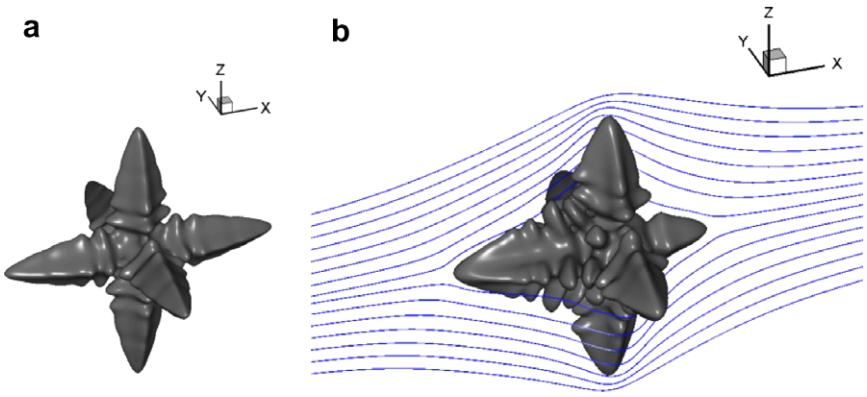

Fig. 8. Effect of forced flow on the morphology for $\Delta = 0.01$: (a) $U^* = 0$; (b) $U^* = 64$.

stream arm directly. The warmer fluid in the front of the transverse arm, which is always coming from the upstream arm, suppresses the growth of the side branches. However, in 3D, the side branches appear from the transversal arms are parallel to the flow. Jeong et al. [13] also obtained a similar result. As shown in Fig. 6, according to the streamlines, the cold fluid from the inlet boundary flows to the transversal arm directly. Therefore, it is anticipated that the side branches from the transversal arms are easily induced by the upstream flow.

We have also conducted the simulation for low supercooling at $\Delta = 0.01$. The simulated morphologies for diffusive and convective growths are shown in Fig. 8(a) and 8(b), respectively; $U^* = 64$ for Fig. 8(b) is needed for a significant flow contribution on the morphology. As shown, the side branching induced by the flow appears along the upstream arm, and some at the upstream side of the transversal arm. This is consistent with the previous experimental observations [23], which were conducted at low undercoolings, and is also similar to the previous 2D results [11,12]. Again, this could be explained by the convective thermal boundary layer as well. At low undercooling, the thermal boundary layer becomes much thicker, and with the current flow structure, the forced flow significantly reduces the thermal boundary layer along the primary arm and the upstream side of the transversal arms. As a result, the side branches are easily induced there.

Therefore, based on the present comparison, care must be taken in using 2D simulations to interpret the real 3D experimental results. Significant difference due to the heat flow can be anticipated, and this is due to the fundamental difference in the flow structure; the 3D flow has more degree of freedoms as a result of the third dimension for the heat flow.

5. Conclusion

2D and 3D adaptive phase field simulations using a finite volume method are carried out for a dendritic growth in a forced flow. The simulated results have compared with the available classic solutions and simulated results, and good agreement is found. The effect of flow on the tip speed and radius, as well as the crystal morphology is investigated, and again they are consistent with the reported simulations and experiments. For the same flow intensity, the effect of flow on 2D and 3D morphologies are also discussed. It is found that the side branches can be easily induced from the transversal arms in the 3D crystal. Apparently, the fundamental difference in the 2D and 3D flow structures is the cause for such different growth morphologies. The 2D and 3D temperature fields near the upstream side of the crystal are also quite different. The thermal gradients remain about the same along the upstream surface of the 3D crystal, while they drop quickly along the 2D crystal as a result of the convective heat transport and the release of heat of fusion. The warmer surrounding in 2D along the transverse arms thus suppresses the growth of side branches from there. On the other hand, the direct cold fluid from the upstream induces side branches from the transversal arms for the 3D crystal. For the case with low undercooling, due to the much thicker thermal boundary layer, the side branching appears along the upstream arm and some on the upstream side of the transverse arms. This is consistent with the experimental observations.

Acknowledgement

This work was supported by the National Science Council of the Republic of China and National Taiwan University through the top projects.

References

[1] G.P. Ivantsov, Temperature field around spherical cylindrical and needle-shaped crystals which grow in supercooled melt, Dokl. Akad. Nauk SSSR 58 (1947) 567–569.
[2] J.S. Langer, Chance and matter, in: J. Souletie, J. Vannimenus, R. Stora (Ed.), Proceedings of the Les Houches Summer School, Session XLVI (North-Holland, Amsterdam, 1987), pp. 629–711.
[3] D. Kessler, J. Koplik, H. Levine, Pattern selection in fingered growth phenomena, Adv. Phys. 37 (1988) 255–339.
[4] Ph. Bouissou, P. Pelce, Effect of a forced flow on dendritic growth, Phys. Rev. A 40 (1989) 6679–6680.
[5] A. Karma, W.-J. Rappel, Phase-field method for computationally efficient modeling of solidification with aritray interface kinetics, Phys. Rev. E 53 (1996) R3017–R3020.
[6] A. Karma, W.-J. Rappel, Quantitative phase-field modeling of dendritic growth in two and three dimensions, Phys. Rev. E 57 (1998) 4323–4349.
[7] A. Karma, W.-J. Rappel, Numerical simulation of three-dimensional dendritic growth, Phys. Rev. Lett. 77 (1996) 4050–4053.
[8] A. Karma, Y.H. Lee, M. Plapp, Three-dimensional dendrite-tip morphology at low undercooling, Phys. Rev. E 61 (2000) 3996–4006.
[9] G. Amberg, Semisharp phase field method for quantitative phase change simulations, Phys. Rev. Lett. 91 (2003) 265505.
[10] N. Provatas, N. Goldenfield, J. Dantzig, Efficient computation of dendritic microstructures using adaptive mesh refinement, Phys. Rev. Lett. 80 (1998) 3308–3311.
[11] C.W. Lan, C.M. Hsu, C. C Liu, Y.C. Chang, Adaptive phase field simulation of dendritic growth in a forced flow at various supercoolings, Phys. Rev. E. 65 (2002) 061601.
[12] C.W. Lan, C.M. Hsu, C. C Liu, Efficient adaptive phase field simulation of dendritic growth in a forced flow at low supercooling, J. Cryst. Growth 241 (2002) 379–386.
[13] J.-H. Jeong, N. Goldenfeld, J.A. Dantzig, Phase field model for three-dimensional dendritic growth with fluid flow, Phys. Rev. E 64 (2001) 041602.
[14] J.-H. Jeong, J.A. Dantzig, N. Goldenfeld, Dendritic growth with fluid flow in pure materials, Metall. Mater. Trans. A 34A (2003) 459–466.
[15] S.-C. Huang, M.E. Glicksman, Fundamentals of dendritic solidfication-I. Steady-state tip growth, Acta Metall. 29 (1981) 701–715.
[16] Y. Lu, C. Beckermann, J.C. Ramirez, Three-dimensional phase-field simulations of the effect of convection on free dendritic growth, J. Crystal Growth 280 (2005) 320–334.

[17] C. Beckermann, H.-J. Diepers, I. Steinbach, A. Karma, X. Tong, Modeling melt convection in phase-field simulations of solidification, J. Comput. Phys. 154 (1999) 468–496.
[18] C.W. Lan, C.M. Hsu, C. C Liu, An adaptive finite volume method for incompressible heat flow problems in solidification, J. Comput. Phys. 178 (2002) 464–497.
[19] S.R. Mathur, J.Y. Murthy, A pressure-based method for unstructured mesh, Num. Heat Transfer B 31 (1997) 195–215.
[20] S.V. Patankar, Numerical Heat Transfer and Fluid Flow, Hemisphere, Washington, D.C., 1980.
[21] C.M. Rhie, W.L. Chow, Numerical study of the turbulent flow past an airfoil with trailing edge separation, AIAA J. 21 (1983) 1525–1532.
[22] X. Tong, C. Beckermann, A. Karma, Velocity and shape selection of dendritic crystals in a forced flow, Phys. Rev. E 61 (2000) R49–R52.
[23] N. Noel, H. Jamgotchian, B. Billia, In situ and real-time observation of the formation and dynamics of a cellular interface in a succinonitrile-0.5 wt% acetone alloy directionally solidified in a cylinder, J. Cryst. Growth 181 (1997) 117–132.